10.1071/CH16614_AC

Australian Journal of Chemistry 2017, 70(5), 505-515

SUPPLEMENTARY MATERIAL

[NiFe]-Hydrogenase synthetic models with redox-active ligands

David Schilter,[A,B,C] *Danielle L. Gray,*[B] *Amy L. Fuller,*[B] *and Thomas B. Rauchfuss*[B]

[A]IBS Center for Multidimensional Carbon Materials, 50 UNIST-gil, Ulsan 44919 (South Korea)
[B]Department of Chemistry, University of Illinois at Urbana-Champaign, 600 S. Goodwin Ave. Urbana, IL 61801, USA
[C]Corresponding author. Email: d.schilter@gmail.com

List of Figures

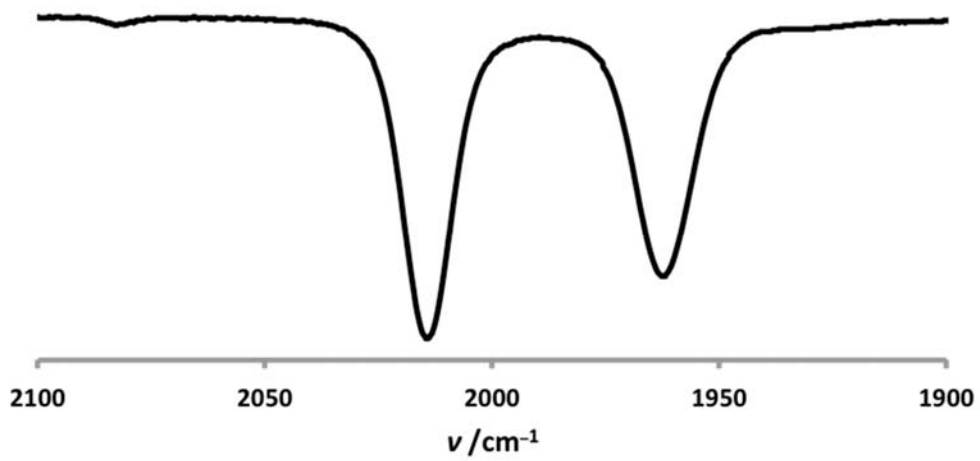

Figure S1. FT-IR spectrum (ν_{CO} region, CH_2Cl_2) of [**1a**(μ-H)]BF_4.

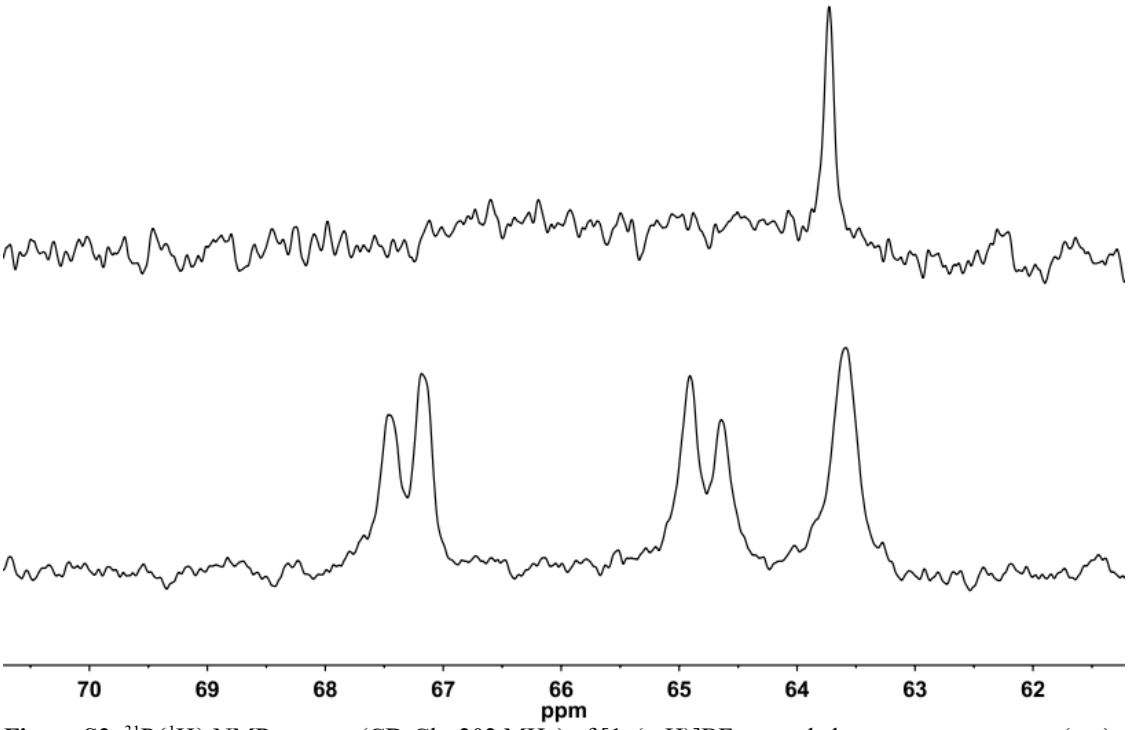

Figure S2. $^{31}P\{^1H\}$ NMR spectra (CD_2Cl_2, 202 MHz) of [**1a**(μ-H)]BF_4 recorded at room temperature (top) and at –28°C (bottom).

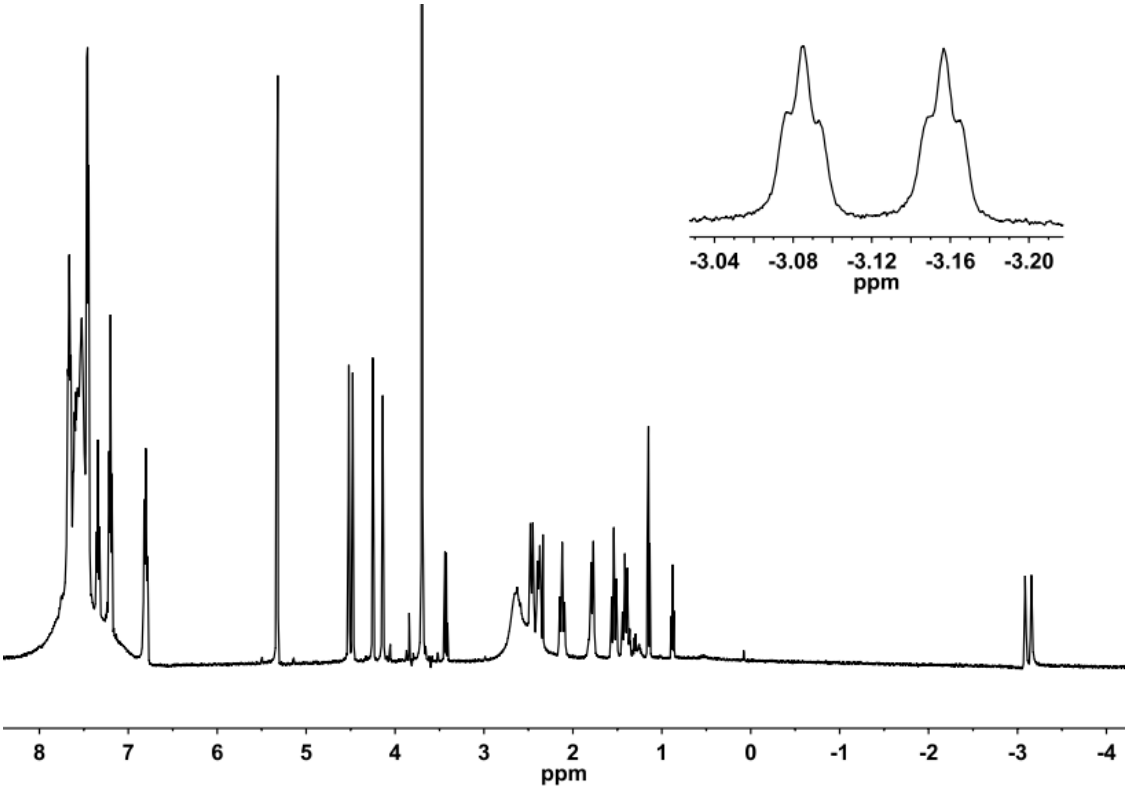

Figure S3. ^{1}H NMR spectrum (CD_2Cl_2, 500 MHz) of [**1a**(μ-H)]BF_4. Resonances at 3.43 (Et_2O), 1.31 (pentane), 1.12 (Et_2O) and 0.89 ppm (pentane) are from impurities in the NMR solvent.

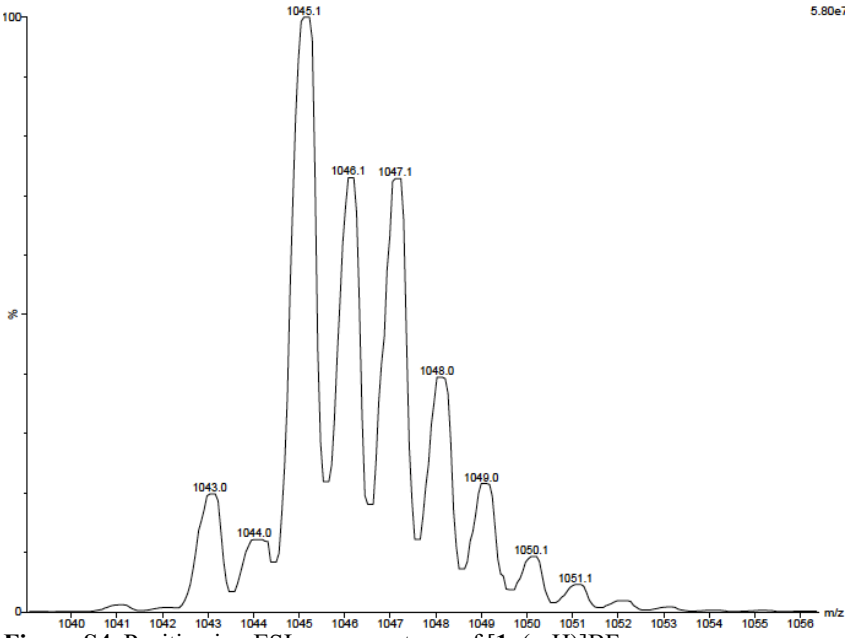

Figure S4. Positive ion ESI mass spectrum of [**1a**(μ-H)]BF_4.

Brown single crystals of [**1a**(μ-H)]$BF_4 \cdot CH_2Cl_2$ formed upon slow diffusion of pentane vapor into a concentrated CH_2Cl_2 solution of [**1a**(μ-H)]BF_4. One crystal was subjected to X-ray diffraction at 173 K, its space group determined as monoclinic $P2_1/c$ ($Z = 4$) with cell parameters: a 12.6528(6) Å, b 33.7738(18) Å, c 12.2942(6) Å, α 90°, β 90.373(4)°, γ 90°. While these preliminary data were of poor quality, they did confirm the atom connectivity within the complex. The Ni-Fe distance in [**1a**(μ-H)]$^+$ (2.662 Å) is similar to that in the analogous triphosphine hydride [(dppe)Ni(pdt)HFe$(CO)_2(PPh_3)]^+$ (2.643 Å), with the monophosphine occupying a basal coordination site *trans* to an S atom in both complexes. The H^- ligand was not resolved in the Fourier difference map. Rather, it was fixed at a distance from Fe1 equivalent to that in the PPh_3 congener. Indirect evidence of the presence of H^- comes from the stereochemistry at the Fe1 site: were the hydride not present, then the mppf ligand would likely occupy an apical position, as it does in the Ni(II)Fe(I) model complexes of the type [(dppe)Ni(pdt)Fe$(CO)_2(PRAr_2)]^+$, including [**2b**]$^+$. In this case, the π-accepting CO ligands are poised *trans* to the π-donating CO groups, no doubt a favorable situation. But this is not the case with [**1a**(μ-H)]$^+$, in which mppf occupied a basal site, ceding its favorable apical position to CO, a ligand that prefers a strong donor *trans* to it, in this case H^-. Lastly, it is noted that the bond distances are consistent with a Ni(II)(μ-H)Fe(II)*Fe(II)* description for this complex, in line with the CO stretching frequencies and the sharpness of the NMR data.

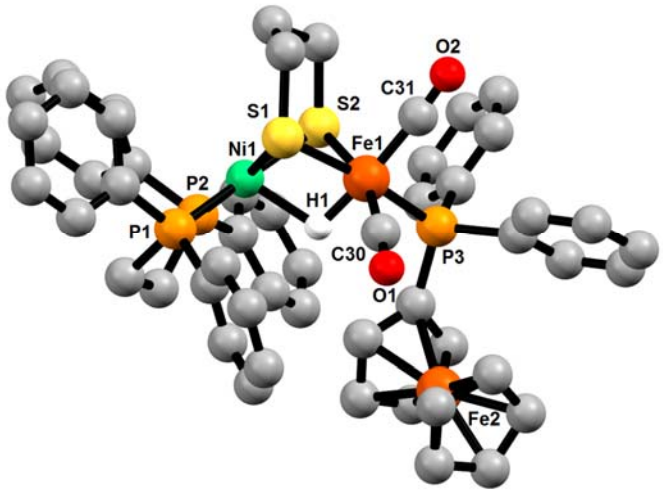

Figure S5. X-ray structure of [**1a**(μ-H)]$BF_4 \cdot CH_2Cl_2$ with the H atoms, disordered BF_4^- anion and CH_2Cl_2 solvate molecule omitted for clarity. Disorder in the Cp ring and two Ph groups of the dppe ligand is also omitted for clarity. Selected distances (Å): Ni1-Fe1, 2.66; Ni1-P1, 2.17; Ni1-P2, 2.17; Ni1-S1, 2.21; Ni1-S2, 2.21; Fe1-S1, 2.31; Fe1-S2, 2.31; Fe1-H1, 1.49; Fe1-C30, 1.79; Fe1-C31, 1.78; Fe1-P3, 2.23; Fe2-C_5H_5(centroid), 1.64; Fe2-$C_5H_4PPh_2$(centroid), 1.72.

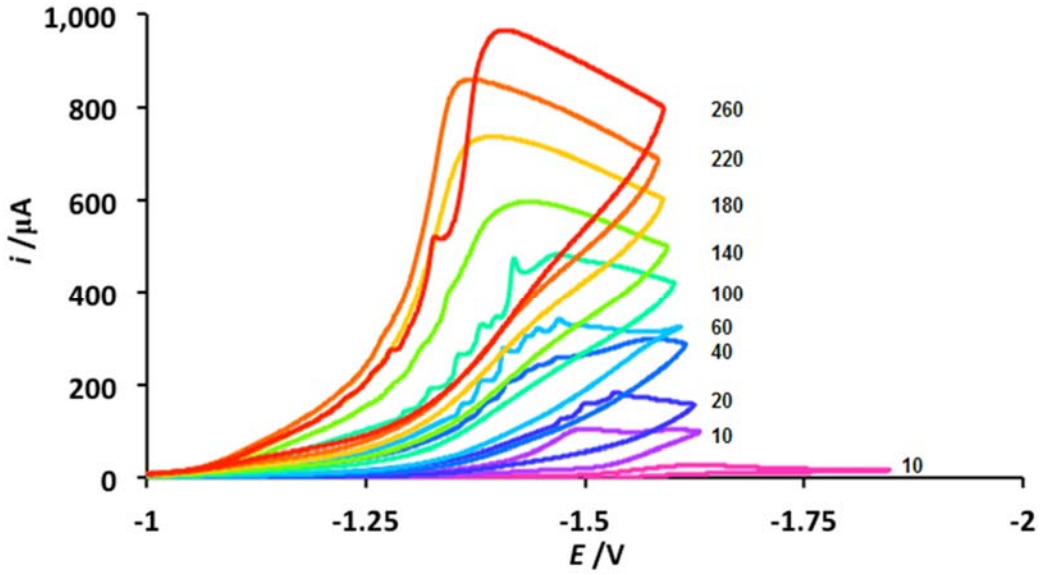

Figure S6. Cyclic voltammograms of [**1a**(μ-H)]BF_4 (1 mM) acquired in the presence of varying molar equivalents of CF_3CO_2H.

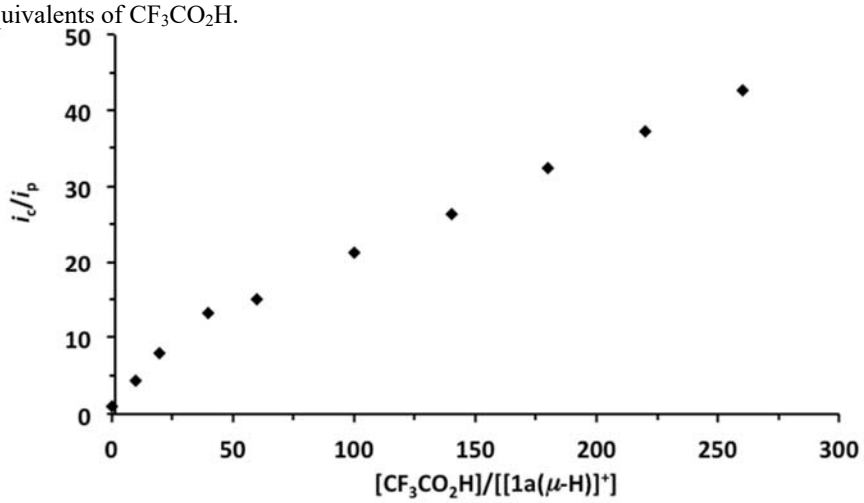

Figure S7. Analysis of the currents observed for reduction of [**1a**(μ-H)]BF_4 (1 mM). The quotient of the current in the presence (i_c) to that in the absence of the acid CF_3CO_2H (i_p) is plotted against the molar ratio of CF_3CO_2H to [**1a**(μ-H)]BF_4. At higher acid concentrations, the wave shifts to more negative potentials, in line with direct reduction of CF_3CO_2H at the glassy carbon electrode.

The turnover frequency k for catalytic hydrogen evolution (n = 2) at a given scan rate v and temperature T can be determined using peak currents in the presence (i_c) and absence of acid (i_p). For catalysis at E_{pc} = –1.37 V (potential at $i_c/2 = E_{pc}$ = –1.33 V):

$$\frac{i_c}{i_p} = \frac{n}{0.4463}\sqrt{\frac{RTk}{Fv}}$$

$$\frac{965\ \mu A}{22.6\ \mu A} = \frac{2}{0.4463}\sqrt{\frac{(8.314\ JK^{-1}mol^{-1})(298\ K)k}{(96485\ Cmol^{-1})(0.1\ JC^{-1}s^{-1})}}$$

$$k\ \approx 350\ s^{-1}$$

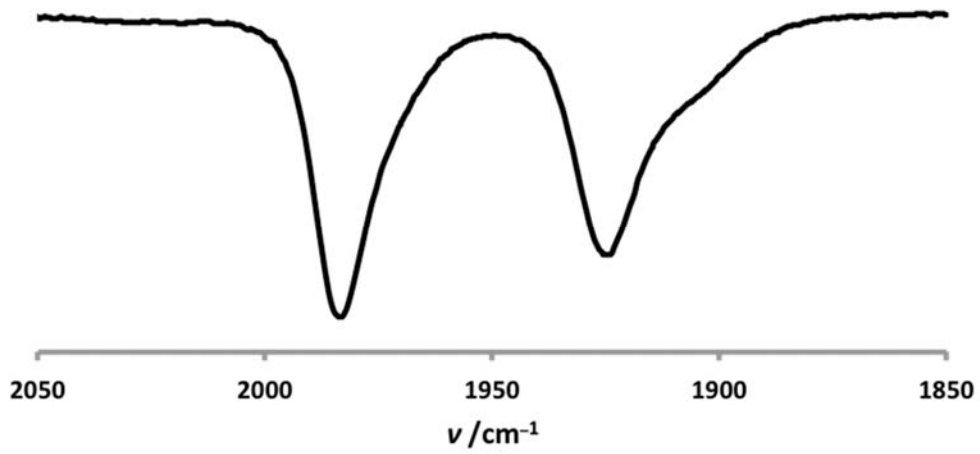

Figure S8. FT-IR spectrum (ν_{CO} region, CH_2Cl_2) of [**1a**]BF_4.

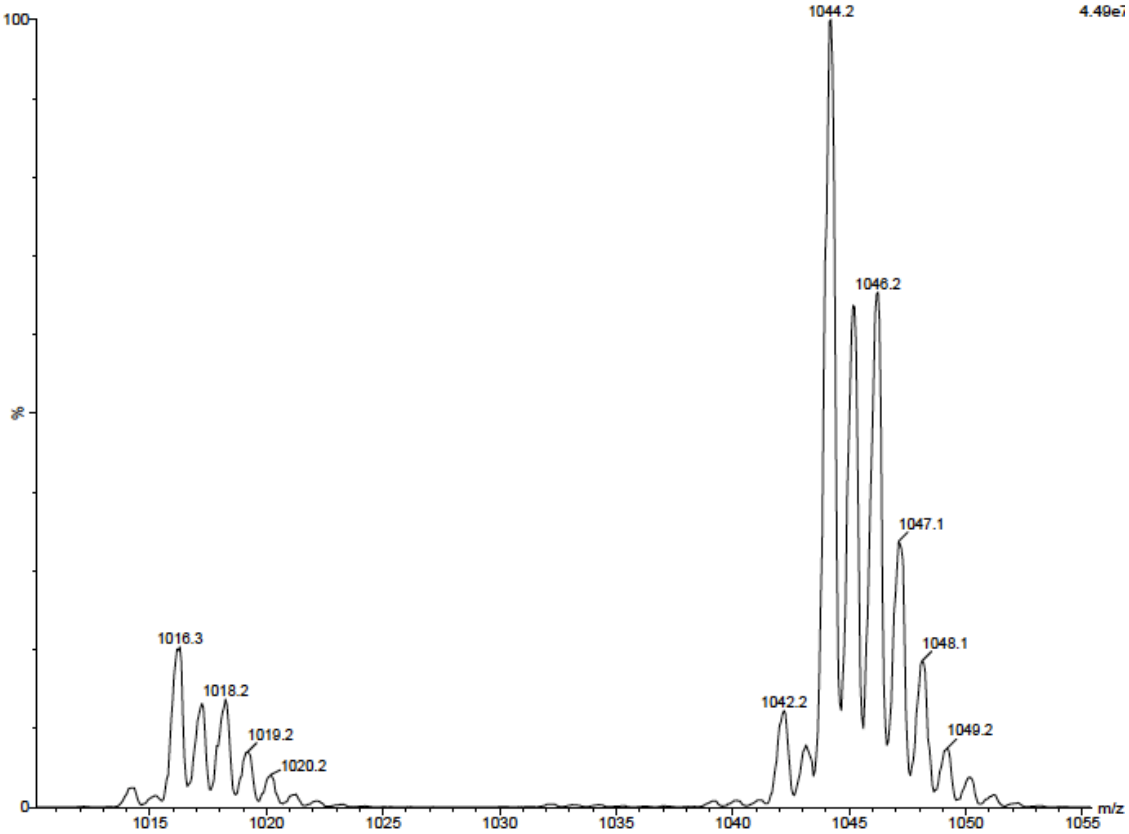

Figure S9. Positive ion ESI mass spectrum of [**1a**]BF_4.

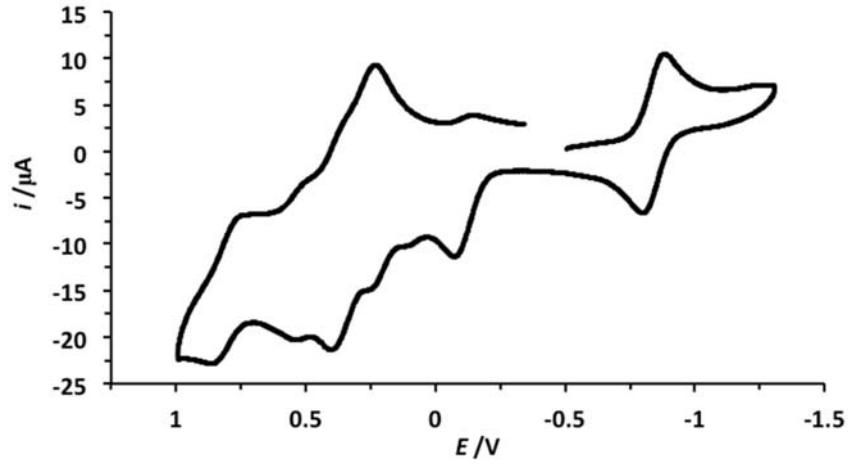

Figure S10. Cyclic voltammogram of [**1a**]BF_4.

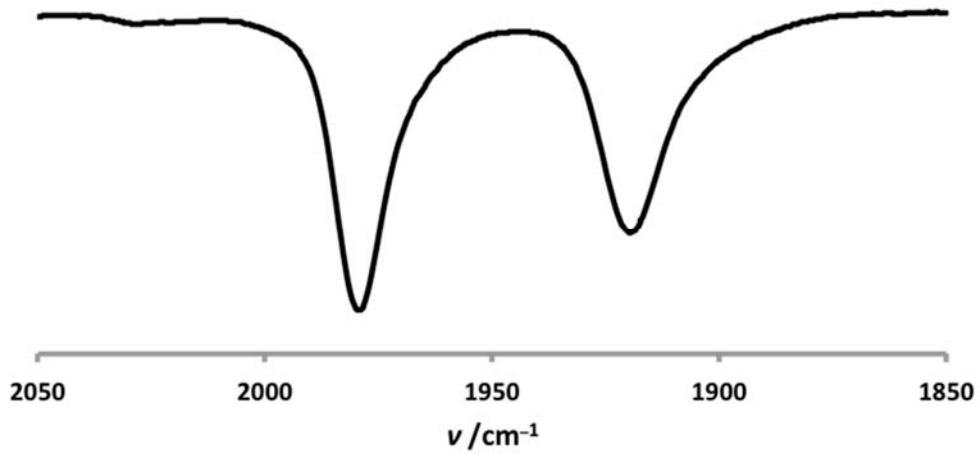

Figure S11: FT-IR spectrum (ν_{CO} region, CH_2Cl_2) of [**1b**]BF_4.

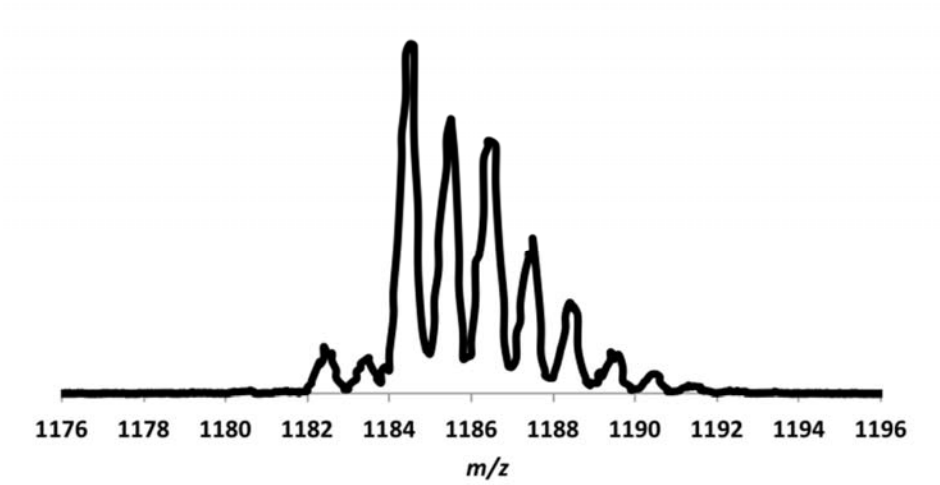

Figure S12: Positive ion ESI mass spectrum of [**1b**]BF_4.

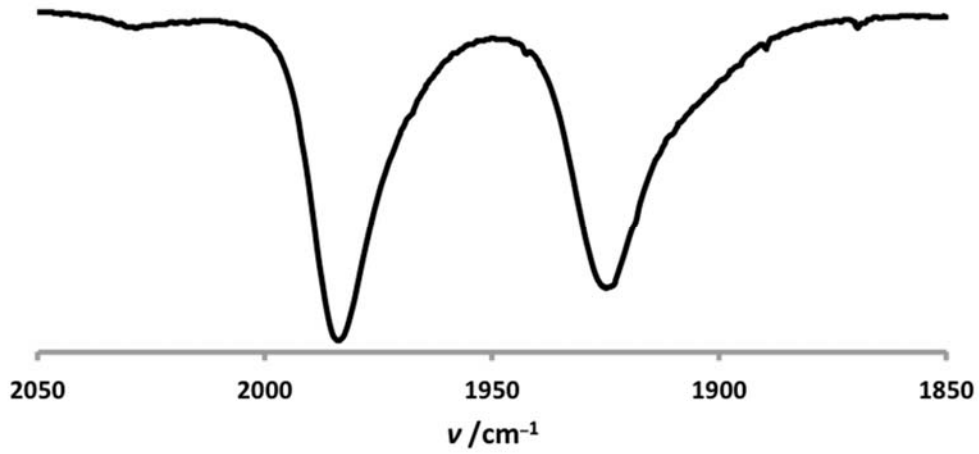

Figure S13: FT-IR spectrum (ν_{CO} region, CH_2Cl_2) of [**1c**]BF_4.

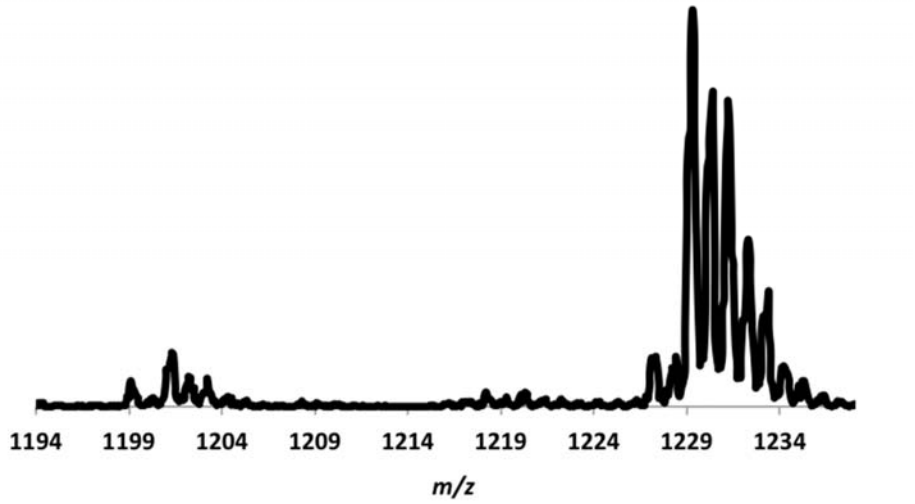

Figure S14. Positive ion ESI mass spectrum of [**1c**]BF_4.

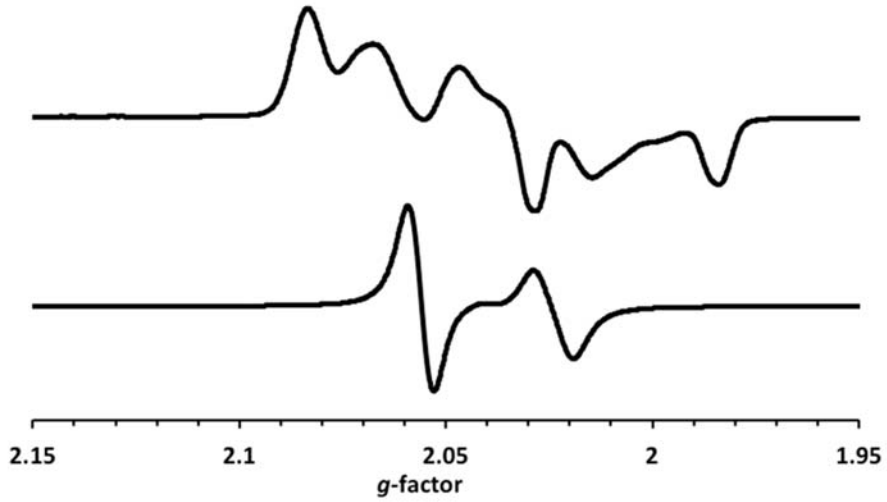

Figure S15. X-band EPR spectra of [**1c**]BF_4 in CH_2Cl_2/PhMe recorded at 110 K (top) and room temperature (bottom).

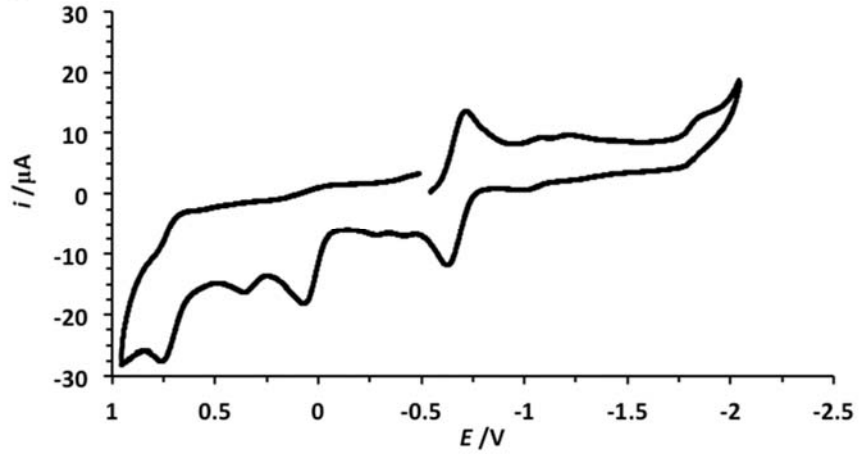

Figure S16. Cyclic voltammogram of [**1c**]BF_4.

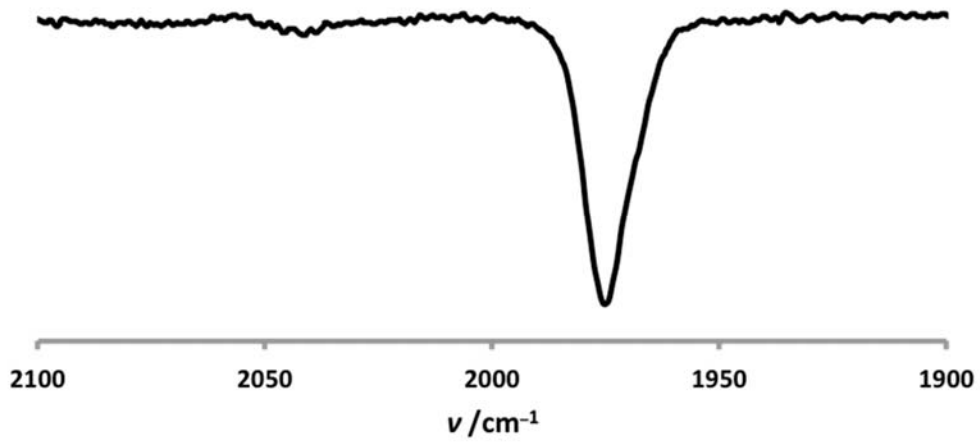

Figure S17. FT-IR spectrum (ν_{CO} region, CH_2Cl_2) of [**1c**]$(BF_4)_2$.

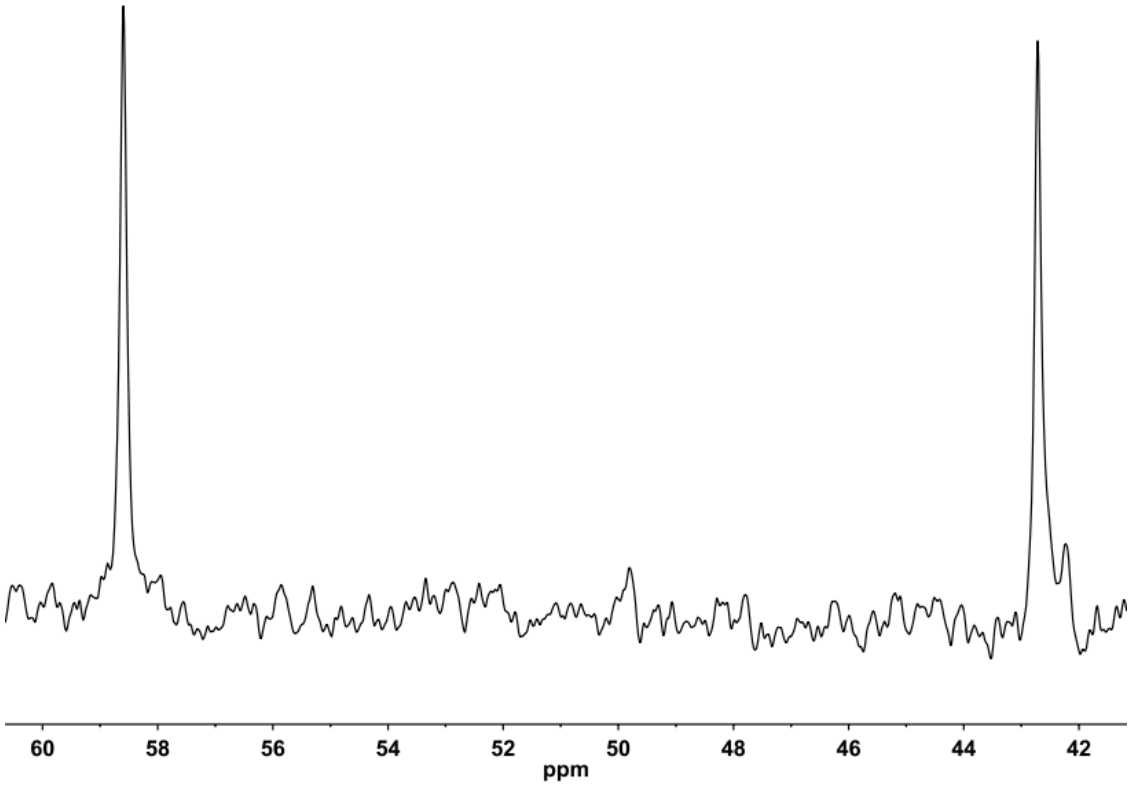

Figure S18. $^{31}P\{^1H\}$ NMR spectrum (CD_2Cl_2, 202 MHz) of [**1c**]$(BF_4)_2$.

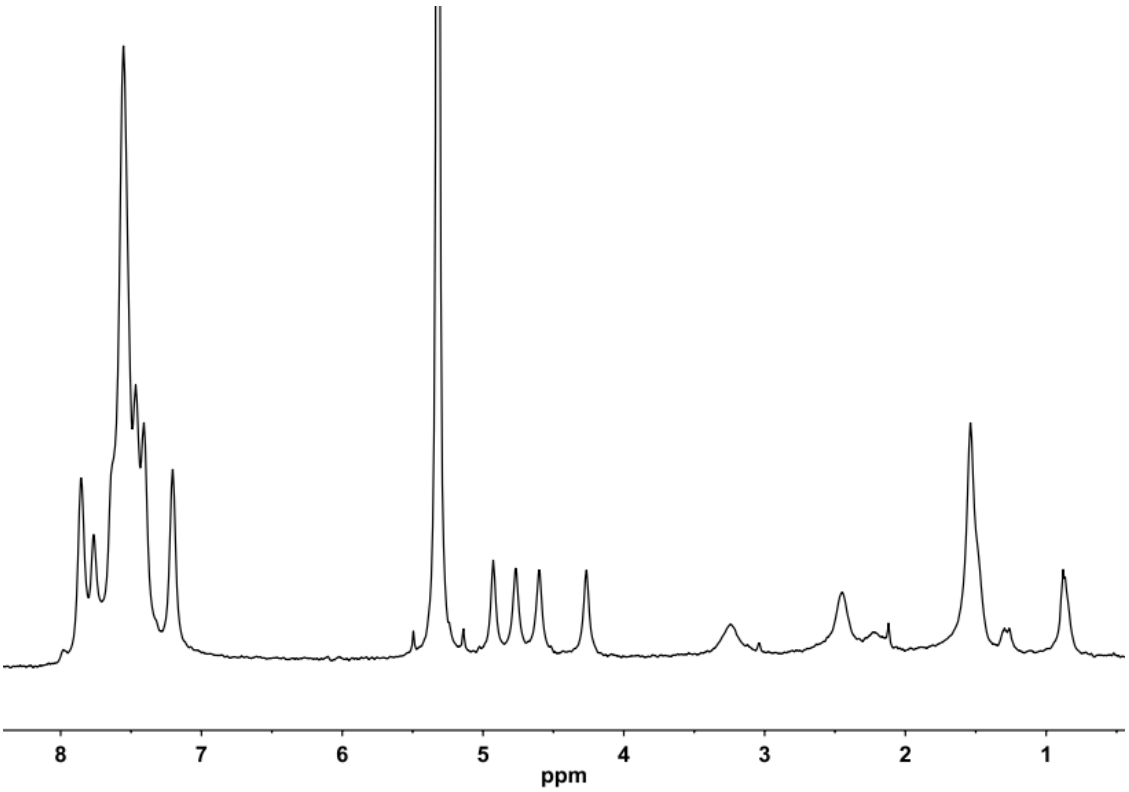

Figure S19. ^{1}H NMR spectrum (CD_2Cl_2, 500 MHz) of [**1c**]$(BF_4)_2$. Resonances at 3.43 (Et_2O), 1.31 (pentane), 1.12 (Et_2O) and 0.89 ppm (pentane) are from impurities in the NMR solvent.

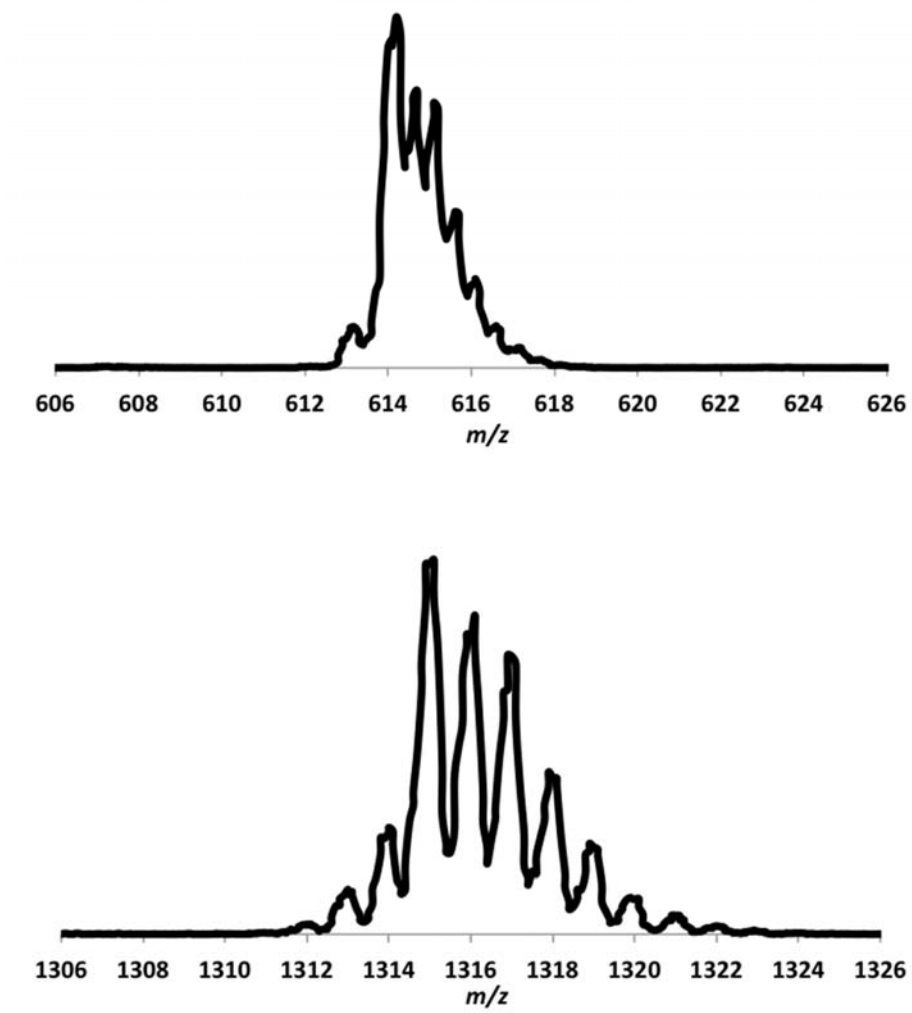

Figure S20: Positive ion ESI mass spectra of [**1c**]$(BF_4)_2$.

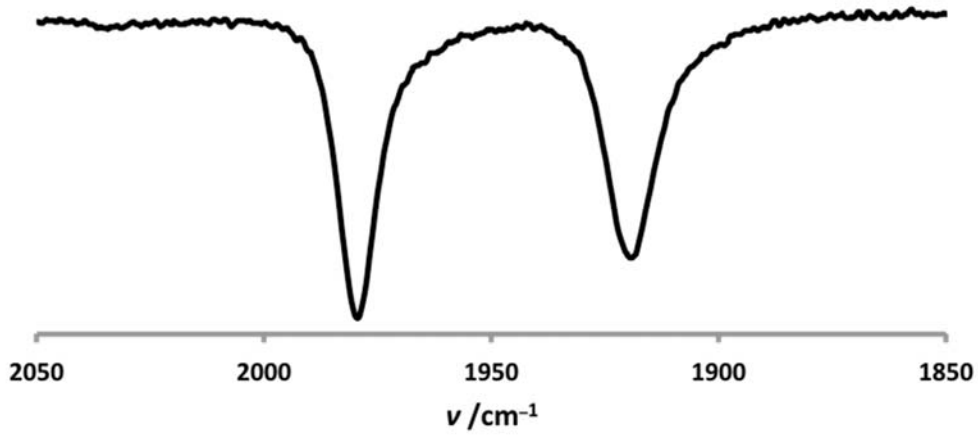

Figure S21. FT-IR spectrum (ν_{CO} region, CH_2Cl_2) of [**2a**]BF_4.

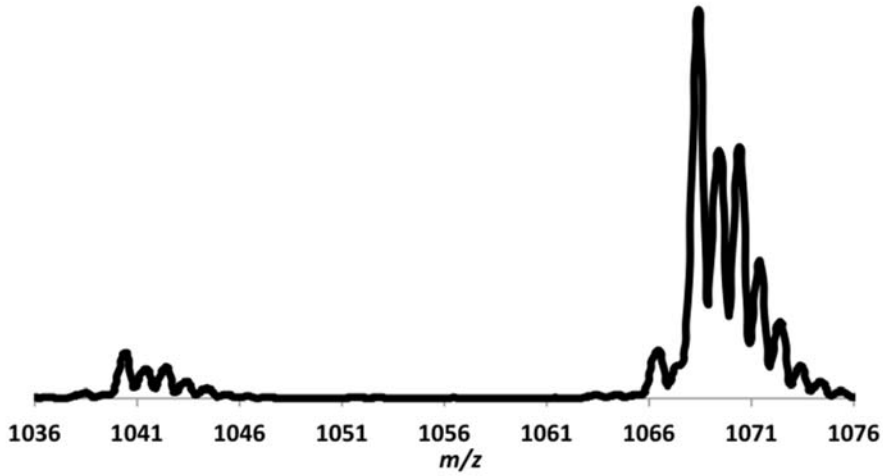

Figure S22. Positive ion ESI mass spectrum of [**2a**]BF_4.

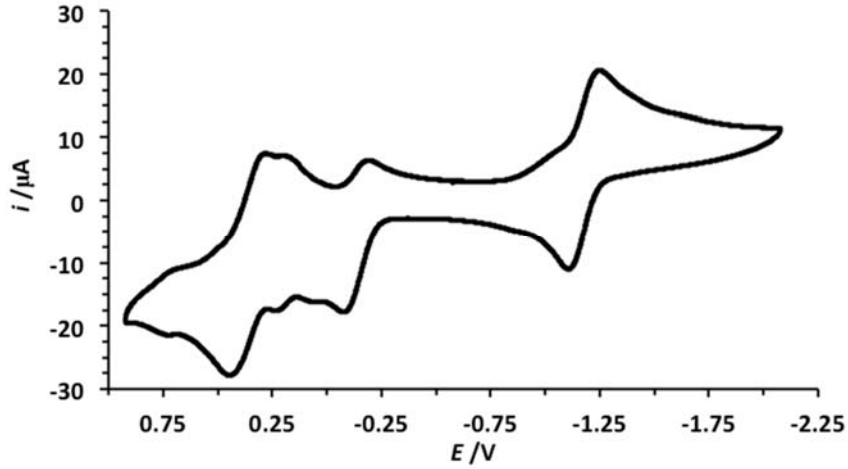

Figure S23. Cyclic voltammogram of [**2a**]BF_4.

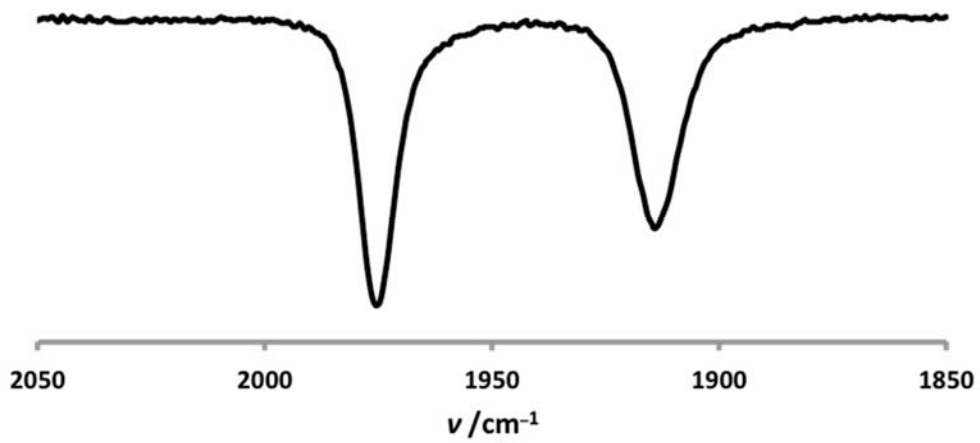

Figure S24. FT-IR spectrum (ν_{CO} region, CH_2Cl_2) of [**2b**]BF_4.

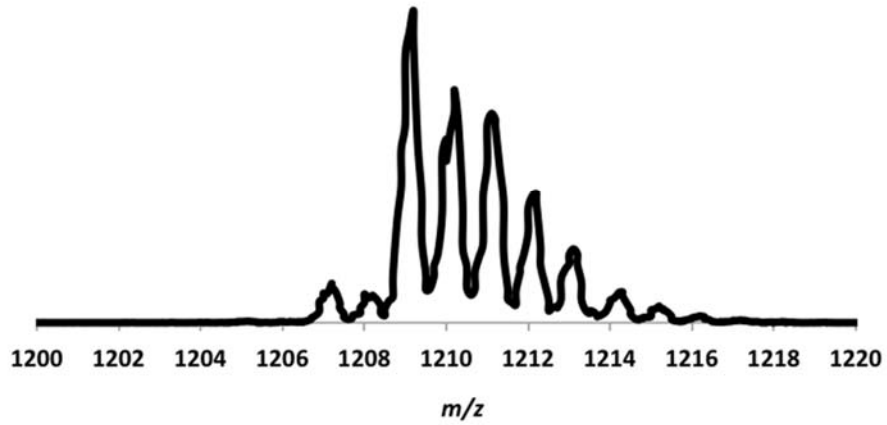

Figure S25. Positive ion ESI mass spectrum of [**2b**]BF_4.

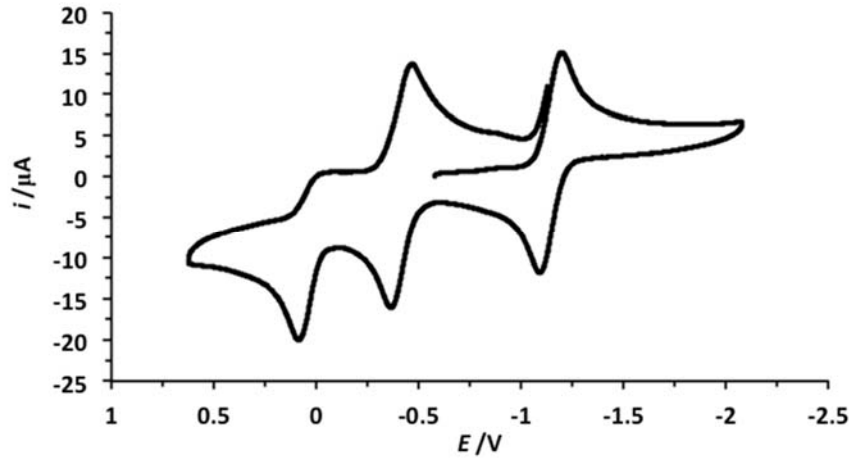

Figure S26. Cyclic voltammogram of [**2b**]BF_4.

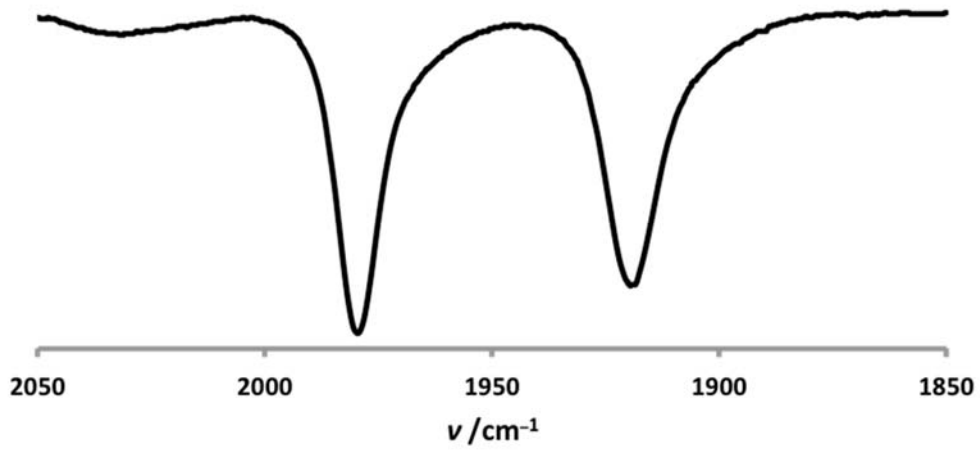

Figure S27: FT-IR spectrum (ν_{CO} region, CH_2Cl_2) of [**2c**]BF_4.

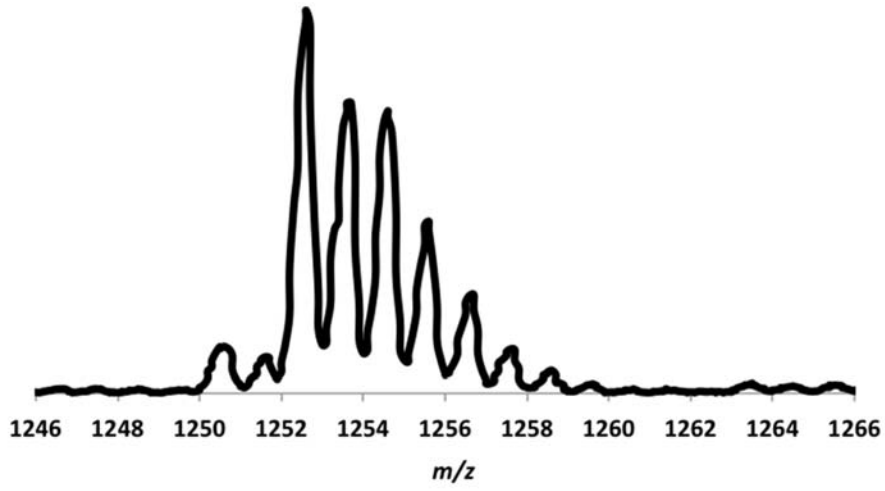

Figure S28. Positive ion ESI mass spectrum of [**2c**]BF_4.

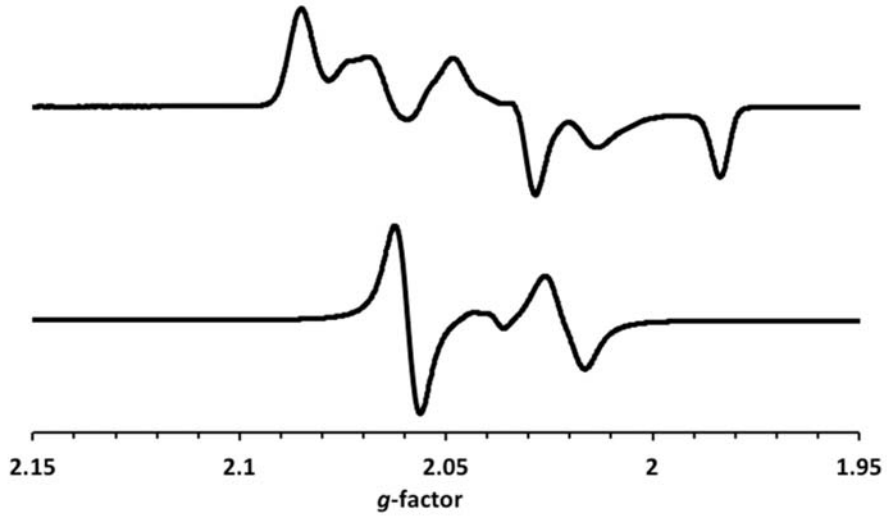

Figure S29. X-band EPR spectra of [**2c**]BF_4 in CH_2Cl_2/PhMe recorded at 110 K (top) and room temperature (bottom).

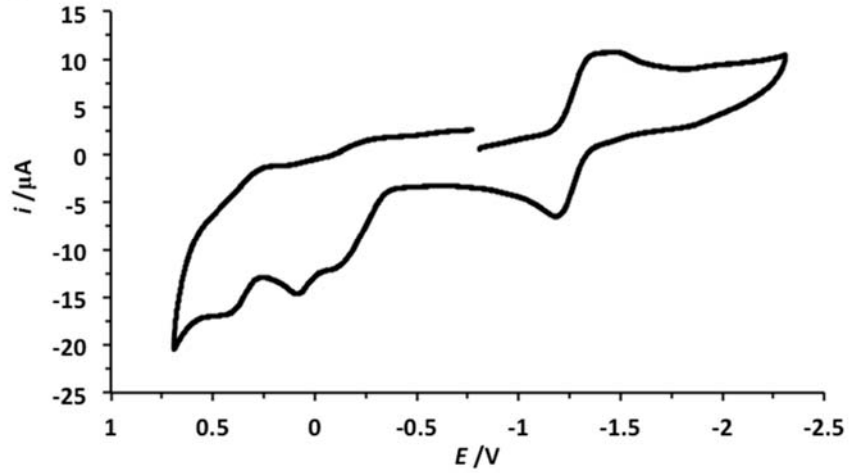

Figure S30. Cyclic voltammogram of [**2c**]BF_4.

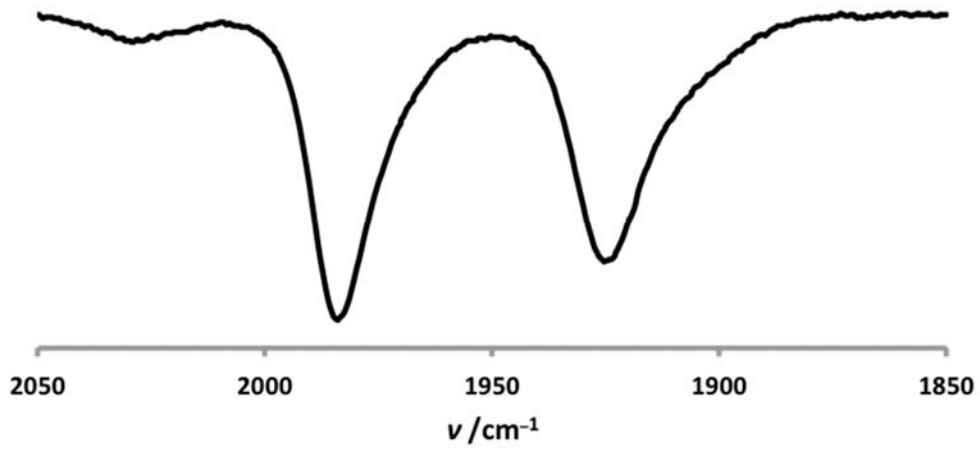

Figure S31: FT-IR spectrum (ν_{CO} region, CH_2Cl_2) of [**3**]$(BF_4)_2$.

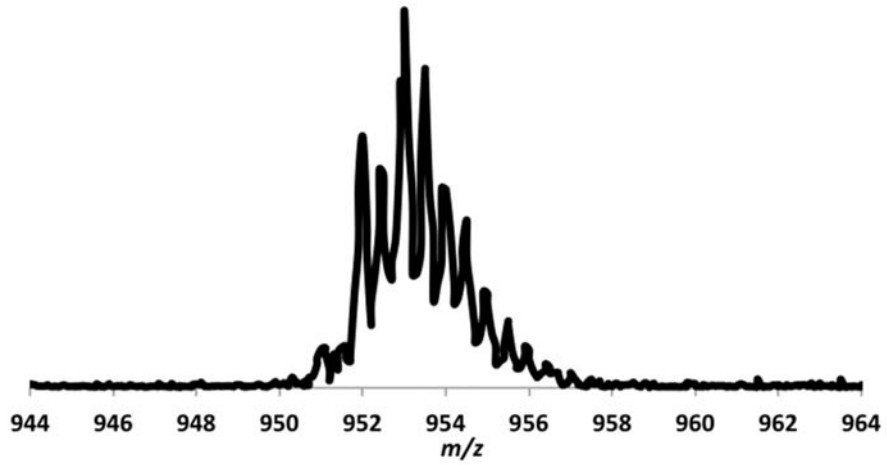

Figure S32. Positive ion ESI mass spectrum of [**3**]$(BF_4)_2$.

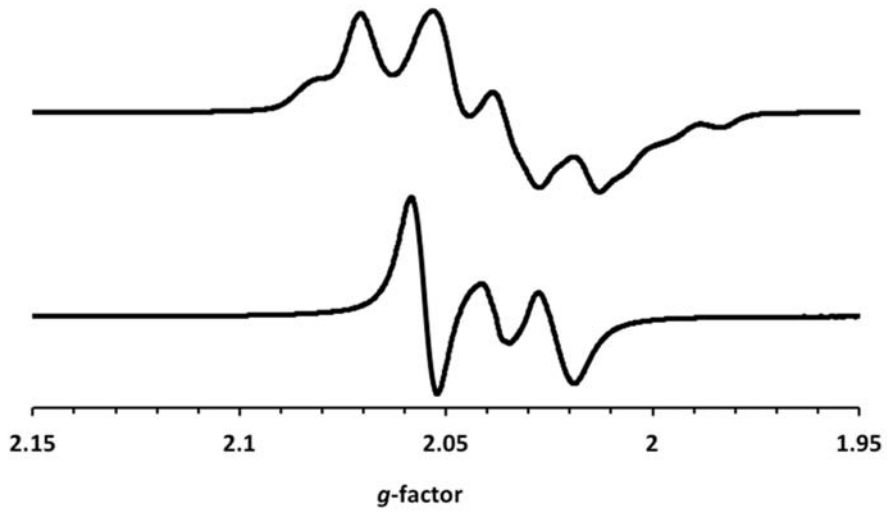

Figure S33. X-band EPR spectra of [**3**]$(BF_4)_2$ in CH_2Cl_2/PhMe recorded at 110 K (top) and room temperature (bottom).

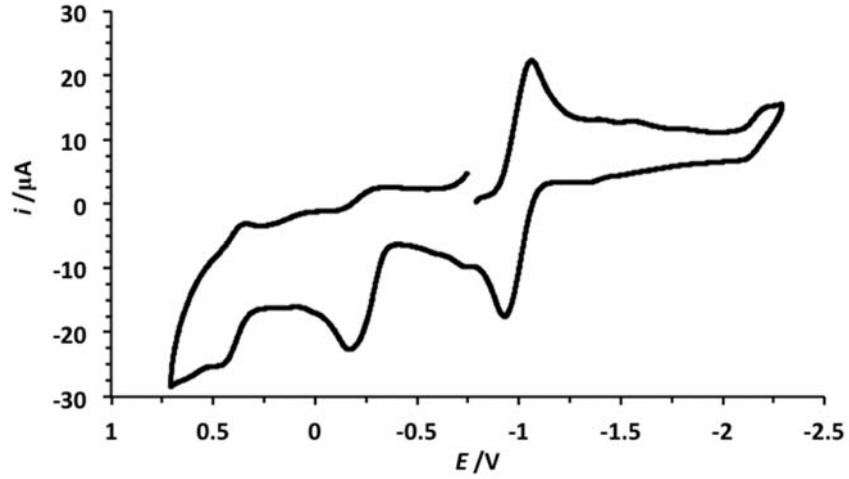

Figure S34. Cyclic voltammogram of [**3**]$(BF_4)_2$.